CrystEngComm

ROYAL SOCIETY OF CHEMISTRY

PAPER

View Article Online
View Journal | View Issue

Cite this: *CrystEngComm*, 2021, **23**, 1604

Four dual-functional luminescent Zn(II)-MOFs based on 1,2,4,5-benzenetetracarboxylic acid with pyridylbenzimidazole ligands for detection of iron(III) ions and acetylacetone†

Yong-Sheng Shi,[a] Qiang Yu,*[a] Jian-Wei Zhang[b] and Guang-Hua Cui *[a]

Four new Zn(II) metal–organic frameworks (MOFs): $\{[Zn(L1)(BTEC)_{0.5}]\cdot 3.1H_2O\}_n$ (**1**), $\{[Zn(L2)_{0.5}(BTEC)_{0.5}]\cdot 1.5H_2O\}_n$ (**2**), $\{[Zn_2(L3)(BTEC)(H_2O)]\cdot H_2O\}_n$ (**3**), and $\{[Zn_2(L4)(BTEC)]\cdot H_2O\}_n$ (**4**) were constructed by selecting N-containing linkers with the Zn(II)/H_4BTEC system (H_4BTEC = 1,2,4,5-benzenetetracarboxylic acid, L1 = 1,4-bis(1-(pyridin-4-ylmethyl)-1*H*-benzo[*d*]imidazol-2-yl)cyclohexane, L2 = 1,4-bis(1-(pyridin-4-ylmethyl)-1*H*-benzo[*d*]imidazol-2-yl)butane, L3 = 1,5-bis(1-(pyridin-4-ylmethyl)-1*H*-benzo[*d*]imidazol-2-yl)pentane, L4 = 1,4-bis(1-(pyridin-4-ylmethyl)-1*H*-benzo[*d*]imidazol-2-yl)methyl) benzene). Structural analyses indicate that **1** exhibits a (3,4)-connected 2D **3,4L13** sheet. **2** manifests a rare (4,4,4)-connected 2D **4,4,4L10** layer. **3** displays an unprecedented (3,3,4,4,4)-connected 3D network based on the point symbol $\{4\cdot8^2\}_2\{4^2\cdot6\cdot8^3\}_2\{4^2\cdot6\}_2\{4^2\cdot8^2\cdot10^2\}\{8^4\cdot12^2\}$ and **4** presents an unusual **4,4,4,6,6T3** 3D network with a 5-node (4,4,4,6,6)-connected network. The structural variety of these Zn(II) MOFs demonstrates that different N-containing ligands can induce the $BTEC^{4-}$ linkers exhibiting various coordination modes, exerting a great influence on the final MOF frameworks. Further, MOFs **1–4** are favorable dual-functional fluorescent sensors for the detection of Fe^{3+}/acetylacetone with high sensitivity and selectivity. To our knowledge, this is the first report of fluorescent MOFs based on L1–L4 ligands for the detection of Fe^{3+} and acac in the naked eye range.

Received 8th November 2020,
Accepted 7th January 2021

DOI: 10.1039/d0ce01619e

rsc.li/crystengcomm

Introduction

Iron(III) ion is not only an important metal ion in living organisms, but also has a huge effect on a number of critical cell functions.[1–3] Deficiency and excess of iron(III) ions in an organism can cause various iron-trafficking, storage, and balance disorders that are strictly regulated, leading to various health risks, such as anemia, pathological disorders, and skin diseases.[4–6] Acetylacetone (acac) is commonly used in organic synthetic intermediates, analytical reagents and other basic raw ingredients.[7–9] However, acac is harmful when exposed to air as a poisonous, explosive, combustible compound, and induces significant environmental issues and human disorders such as dizziness, sicchasia, unconsciousness, and so forth.[10–12] How to efficiently detect iron(III) ions/acac is therefore an incredibly critical problem. Despite the various analytical techniques currently being developed for the determination of iron(III) ions and acac, such as spectrophotometry, voltammetry, and atomic absorption spectroscopy, however, these methods easily be interfered by other environmental substances.[13–15] Therefore, it is very important to establish new methods that can be conveniently extended to detect iron(III) ions and acac exclusively.

Due to their charming topological networks and tremendous potential applications, metal–organic frameworks (MOFs) have undergone enormous growth in recent decades.[16–19] Many MOFs were used as convincing and promising sensors for the identification of small organic molecules and metal ions.[20–22] Compared to traditional detection, this type of sensor typically exhibits clear advantages in terms of sensitivity, response time and operability.[23,24] Some considerable progress has been found based on the rational selection of metal ions and organic ligands as well as structural characteristics, especially for MOF-supported fluorescent probes.[25,26] Accordingly, MOF-based fluorescent sensors are also likely to be a judicious alternative for the efficient detection of iron(III) ions and acac. However, it has

[a] *College of Chemical Engineering, Hebei Key Laboratory for Environment Photocatalytic and Electrocatalytic Materials, North China University of Science and Technology, No. 21 Bohai Road, Caofeidian New-City, Tangshan, Hebei, 063210, P. R. China. E-mail: yuqiang@ncst.edu.com, tscghua@126.com; Fax: +86 0315 8805462; Tel: +86 0315 8805460*

[b] *Tangshan Normal University, Tangshan, Hebei, 063210, P. R. China*

† Electronic supplementary information (ESI) available. CCDC 2041699–2041702 contain the supplementary crystallographic data for MOFs **1–4**. For ESI and crystallographic data in CIF or other electronic format see DOI: 10.1039/d0ce01619e

been confirmed that the low stability of MOFs in aqueous environments typically limits their sensing impact on target metal ions in a large degree.[27,28] So far, only a few sensors based on MOFs have been recorded that can maintain their stability in water or under humid conditions. It has therefore always been a major challenge to increase the water stability of MOF-based sensors.[29,30]

Motivated by the previously mentioned aspects, 1,2,4,5-benzenetetracarboxylic acid (H_4BTEC), bis(benzimidazole) derivatives and Zn(II) ions were elaborately chosen as organic ligands and metal nodes to construct MOF-based fluorescent sensors from the following considerations: 1) d^{10} transition metal ions can be altered to fluoresce and have become the most widely selected metal ions for synthesis luminescent MOF applications;[31] 2) L1–L4 ligands were designed and synthesized with $-CH_2-$, benzimidazole rings, pyridine rings and –C═N multiple spacers and employ the advantages of increased conformational flexibility and hydrogen bonding sites;[32] 3) there are multiple coordination sites for H_4BETC and L1–L4 ligands, providing a variety of coordination modes, and combining these O-donors and N-donors is easy to form structurally stable target MOFs.[33] As a result, four new fluorescent MOFs, namely, $\{[Zn(L1)(BTEC)_{0.5}]\cdot 3.1H_2O\}_n$ (**1**), $\{[Zn(L2)_{0.5}(BTEC)_{0.5}]\cdot 1.5H_2O\}_n$ (**2**), $\{[Zn_2(L3)(BTEC)(H_2O)]\cdot H_2O\}_n$ (**3**), $\{[Zn_2(L4)(BTEC)]\cdot H_2O\}_n$ (**4**) were synthesized (H_4BTEC = 1,2,4,5-benzenetetracarboxylic acid, L1 = 1,4-bis(1-(pyridin-4-ylmethyl)-1*H*-benzo[*d*]imidazol-2-yl)cyclohexane L2 = 1,4-bis(1-(pyridin-4-ylmethyl)-1*H*-benzo[*d*]imidazol-2-yl)butane, L3 = 1,5-bis(1-(pyridin-4-ylmethyl)-1*H*-benzo[*d*]imidazol-2-yl)pentane, L4 = 1,4-bis((1-(pyridin-4-ylmethyl)-1*H*-benzo[*d*]imidazol-2-yl)methyl)benzene). On the basis of structural characterization and discussion, the fluorescence sensing behaviors of MOFs **1–4** towards metal cations (Fe^{3+}) and acac were investigated. MOFs **1–4** exhibit good sensing efficiency as chemosensors with high selectivity, stability and recyclability and exceedingly low detection limits.

Experimental

Materials and methods

All reagents and solvents were commercially available and can be used without further purification. L1–L4 were purchased from Jinan Henghua Sci. & Tec. Co., Ltd. The FT-IR spectra were recorded from a Bruker VERTEX 80V FT-IR spectrophotometer in the 4000–400 cm^{-1} region. Powder X-ray diffraction (PXRD) patterns were recorded on a Rigaku D/Max-2500 X-ray powder diffractometer (Cu-Kα, 1.5418 Å). Elemental analyses were performed on a PerkinElmer 240 C elemental analyzer. The fluorescence spectra were collected with a Hitachi F-7000 spectrophotometer at room temperature. Thermogravimetric analysis (TGA) data were collected with a NETZSCH TG 209 thermal analyzer in N_2 at a heating rate of 10 °C min^{-1} in the range of 25–700 °C. N_2 adsorption at 77 K was performed on a 3H-2000PM1 analyzer. The morphology of the prepared materials was observed using a transmission electron microscope (TEM, Hitachi HT7700) and a spherical aberration correction electron microscope (Titan G260-300) equipped with an energy dispersive X-ray spectroscopy (EDX) detector (Bruker Nano GmbH, Germany) was used to analyze the elements.

Synthesis of $\{[Zn(L1)(BTEC)_{0.5}]\cdot 3.1H_2O\}_n$ (1)

The starting materials were L1 (49.8 mg, 0.1 mmol), H_4BTEC (50.8 mg, 0.2 mmol) $Zn(OAc)_2\cdot 2H_2O$ (43.9 mg, 0.2 mmol) and H_2O (10 mL). The mixture was placed in a 25 mL Teflon-lined stainless-steel reactor, which was heated at 140 °C for 3 days and then slowly cooled to room temperature at a rate of 5 °C h^{-1}. Colorless block crystals of **1** were collected in 48% yield based on Zn. Anal. calcd for $C_{37}H_{36}N_6O_{7.5}Zn$ (Fw = 745.17): C, 59.58; H, 4.83; N, 11.27. Found (%): C, 58.94; H, 4.63; N, 11.14. IR: 3380 w, 1595 s, 1505 w, 1642 s, 1437 s, 1400 s, 1361 m, 1279 s, 1114 m, 869 w, 758 m.

Synthesis of $\{[Zn(L2)_{0.5}(BTEC)_{0.5}]\cdot 1.5H_2O\}_n$ (2)

2 was obtained by an analogous method to **1**, using L2 (47.2 mg, 0.1 mmol) instead of L1. Colorless block crystals of **2** were collected (yield: 46.3% based on Zn). Anal. calcd for $C_{20}H_{18}N_3O_{5.5}Zn$ (Fw = 453.74): C, 52.94; H, 3.97; N, 9.26. Found (%): C, 53.11; H, 3.21; N, 7.96. IR: 3426 w, 1594 s, 1507 w, 1467 s, 1430 s, 1406 s,1350 m, 1302 m, 1279 s, 1114 m, 882 w, 738 m.

Synthesis of $\{[Zn_2(L3)(BTEC)(H_2O)]\cdot H_2O\}_n$ (3)

3 was obtained by an analogous method to **1**, using L3 (48.6 mg, 0.1 mmol) instead of L1. Colorless block crystals of **3** were collected (yield: 47.2% based on Zn). Elemental analysis (%) calcd for $C_{41}H_{36}N_6O_{10}Zn_2$, (Fw = 903.53): C, 54.50; H, 4.02; N, 9.30. Found (%): C, 54.21; H, 3.89; N, 8.54. IR: 3464 w, 1608 s, 1469 w, 1448 m, 1442 s, 1413 s, 1357 s, 1313 s, 1132 m, 852 w, 751 m.

Synthesis of $\{[Zn_2(L4)(BTEC)]\cdot H_2O\}_n$ (4)

4 was obtained by the same method as **1**, using L4 (52.0 mg, 0.1 mmol) instead of L1. Colorless block crystals of **4** were obtained (yield: 41.8% based on Zn). Elemental analysis (%) calcd for $C_{27}H_{18}N_3O_9Zn_2$, (Fw = 659.18): C, 49.19; H, 2.75; N, 6.37. Found (%): C, 49.01; H, 2.85; N, 6.46. IR: 3566 w, 1616 s, 1594 w, 1542 s, 1506 s, 1434 s, 1400 m, 1333 m, 1279 s, 1292 s, 1114 m, 882 w, 756 m.

Single-crystal X-ray structure determination of MOFs 1–4

The single-crystal structure data of MOFs **1–4** were collected on a Rigaku XtaLabMini diffractometer with Mo-Kα radiation (λ = 0.71073 Å) at room temperature; the reflection data were machined by utilizing the CrysAlisPro program (version 1.171.38.43).[34] The crystal was kept at 293(2) K during data collection by using Olex2;[35] the structure was solved with Olex2.solve and further refined by the full-matrix least squares method on F^2 by using SHELXL (v. 2018/3).[36,37] All ordered non-hydrogen atoms were found from difference Fourier maps and refined with anisotropic thermal parameters. The H atoms of the organic ligands were generated theoretically and refined isotropically with fixed thermal factors. The

disordered lattice H_2O molecules (1.5 for **1**, 1 for **2**, **3** and 3.1 for **4**, respectively) were flattened from their diffraction data using the SQUEEZE routine of PLATON.[38] Crystallographic data and structure refinement parameters for MOFs **1–4** are summarized in Table S1.† Selected bond lengths and bond angles are given in Table S2 in the ESI.†

Results and discussion

General properties

The IR spectra (Fig. S1†) display the ν(O–H) bands of the free water molecules in MOFs **1–4** which are located at 3380, 3426, 3397, and 3401 cm^{-1}, respectively.[39] The asymmetric and symmetric stretching vibrations of the carboxyl groups can be attributed to the strong peaks at 1462–1616 cm^{-1} and 1316–1442 cm^{-1}, respectively. The [ν_{as}(COO)–ν_s(COO)] values were determined to be in the range of 15 and 297 cm cm^{-1} in MOFs **1–4**, indicating that multiple coordination types are adopted by the carboxyl groups of $BTEC^{4-}$ ligands.[40,41] There is no strong absorption band about 1700 cm^{-1} in MOFs **1–4**, indicating that the –COOH groups are completely deprotonated in the $BTEC^{4-}$ ligands.[42] The bands at 1505–1542 cm^{-1} are assigned to the C=N stretching vibration of benzimidazole rings in MOFs **1–4**.[43]

Thermogravimetric experiments with N_2 were performed at 25–800 °C to evaluate the stability of MOFs **1–4** (Fig. S2†). From room temperature to 300 °C, the TGA curve displays a steady plateau, suggesting that MOFs **1–4** are stable up to 300 °C, and then the entire framework starts to decompose upon further heating. Table S3† displays the results for MOFs **1–4**.

The analysis of the experimental and simulated PXRD spectra (Fig. S3†) of MOFs **1–4** indicates that the diffraction peak positions are clear, suggesting that MOFs **1–4** are pure phases and do not contain impurities. The disparity in curve amplitude is due to the crystals' desired direction of action. Simultaneously, to check the chemical stabilities of MOFs **1–4**, their powder specimens were treated with room temperature water, ice water, boiling water, concentrated HCl aqueous solution and NaOH aqueous solution, respectively (Fig. S4†). After soaking in these solutions for 24 hours, the PXRD patterns of MOFs **1–4** show that the retained crystallinity and unchanged structure are in different pH ranges (pH 3–11 for **1**, pH 3–12 for **2**, pH 3–11 for **3** and pH 4–12 for **4**). However, in strongly acidic or alkaline water, MOFs **1–4** show poor stability, which indicates that MOFs **1–4** possess high stability in a certain pH range (Fig. S5†).

The specific surface area and porosity are two important physical properties that affect the quality and purpose of a material; therefore, it is important to accurately measure these parameters. The adsorption performance of MOFs **1–4** was tested with N_2 at 77 K (Table S4†). The calculated BET surface areas are 11.339, 2.301, 8.608, and 12.002 $m^2\ g^{-1}$ for MOFs **1–4**, respectively. The total pore volumes are 0.0643, 0.0198, 0.0494, and 0.0664 $cm^3\ g^{-1}$ for MOFs **1–4**, respectively.

Crystal structure of MOFs 1–4

MOFs **1–4** all crystallize in the triclinic $P\bar{1}$ space group and the monoclinic system. Since **1**/**2** or **3**/**4** have similar structures, the focus was on the detailed description of the structure of **1** and **3**, and the structure description of **2** and **4** was moved to the ESI† (Fig. S7, S9, S31 and S32).

The asymmetric unit of **1** contains one Zn(II) atom, one L1 ligand, half a $BTEC^{4-}$ anion ligand and 3.1 free water molecules (Fig. 1a). The Zn1 center adopts a square pyramidal coordination geometry and is five-coordinated by three O atoms of two carboxylate groups from a $BTEC^{4-}$ anion (Zn(1)–O(1) = 1.940(5) Å, Zn(1)–O(3)A/O(4)A = 1.959(3) Å; symmetry code: A: $3-x$, $2-y$, $-z$), and two pyridyl N atoms from the L1 ligand (Zn(1)–N(3) = 2.073(5) Å, Zn(1)–N(6)B = 2.064(3) Å; symmetry code: B: $2-x$, $1-y$, $1-z$). The coordination angles around Zn1 are in the region of 93.0(2)–132.4(2)°, which are all in the expected range compared to the reported Zn-MOFs in the literature[44] (Table S2†).

In MOF **1**, the carboxylate groups of $BTEC^{4-}$ anions all adopt a $(\kappa^1\text{-}\kappa^0)\text{-}(\kappa^1\text{-}\kappa^1)\text{-}(\kappa^1\text{-}\kappa^0)\text{-}(\kappa^1\text{-}\kappa^1)\text{-}\mu_4$ coordination mode to bind four center Zn(II) ions. Each Zn(II) atom is coordinated with two carboxylates from two $BTEC^{4-}$ anions to produce a 1D straight-like line (Fig. S6a†). Each $(\kappa^0)\text{-}(\kappa^1)\text{-}(\kappa^0)\text{-}(\kappa^1)\text{-}\mu_2$ bridging L1 ligand adopts a *cis*-conformation to bridge the neighboring Zn(II) centers to give an infinite binuclear dimer ring [$Zn_2(L1)_2$] with a non-bonding Zn(II)···Zn(II) distance of 13.499(2) Å (Fig. 1b). Moreover, these adjacent 1D straight-like lines are further supported by the flexible bridging L1 ligands as pillars to produce a 2D sheet (Fig. 1c and S6a†). To gain better insight into the network of **1**, the complicated 2D framework was simplified using ToposPro software.[45] Obviously, $BTEC^{4-}$ anions (red spheres) and Zn(II) ions (cyan spheres) can be considered as four-connected nodes and three-connected nodes, respectively, while L1 ligands can be regarded as linkers (cyan lines). Thus, the sheet of **1** forms a dual-node 3,4-connected **3,4L13** network with a symbol of $\{4\cdot6^2\}_2\{4^2\cdot6^2\cdot8^2\}$ (Fig. 1d and S6b†).

The asymmetric unit of **3** consists of two Zn(II) ions, one L3 ligand, two kinds of half $BTEC^{4-}$ anions, one lattice water molecule and one unbonded water molecule (Fig. 2a). Zn1 centers are in a [$ZnNO_3$] arrangement, exhibiting a distorted tetrahedral geometry. The coordination geometry of the Zn1 ion is constituted by four atoms, including two oxygen atoms from two $BTEC^{4-}$ anions (O1, O5), one oxygen atom from a coordinated water molecule (O9) and one imidazolyl nitrogen atom (N1) from one L3 ligand. The coordination environment of Zn2 is completely different from that of Zn1, surrounded by three oxygen atoms from two $BTEC^{4-}$ anions (O3A, O4A and O7; symmetry code: A: $1+x$, y, z) and two nitrogen atoms (N4B, N6C; symmetry code: B: $1+x$, $1+y$, z, C: $2-x$, $1-y$, $1-z$) from two different L3 ligands, resulting in a distorted [ZnN_2O_3] square pyramidal coordination geometry. The Zn–O/Zn–N bond distances vary from 1.928(2) to 1.965(2) Å and 1.989(2) to 2.086(2) Å, respectively. The bond lengths around Zn(II) ions range from 96.1(7) to 127.2(7)°.

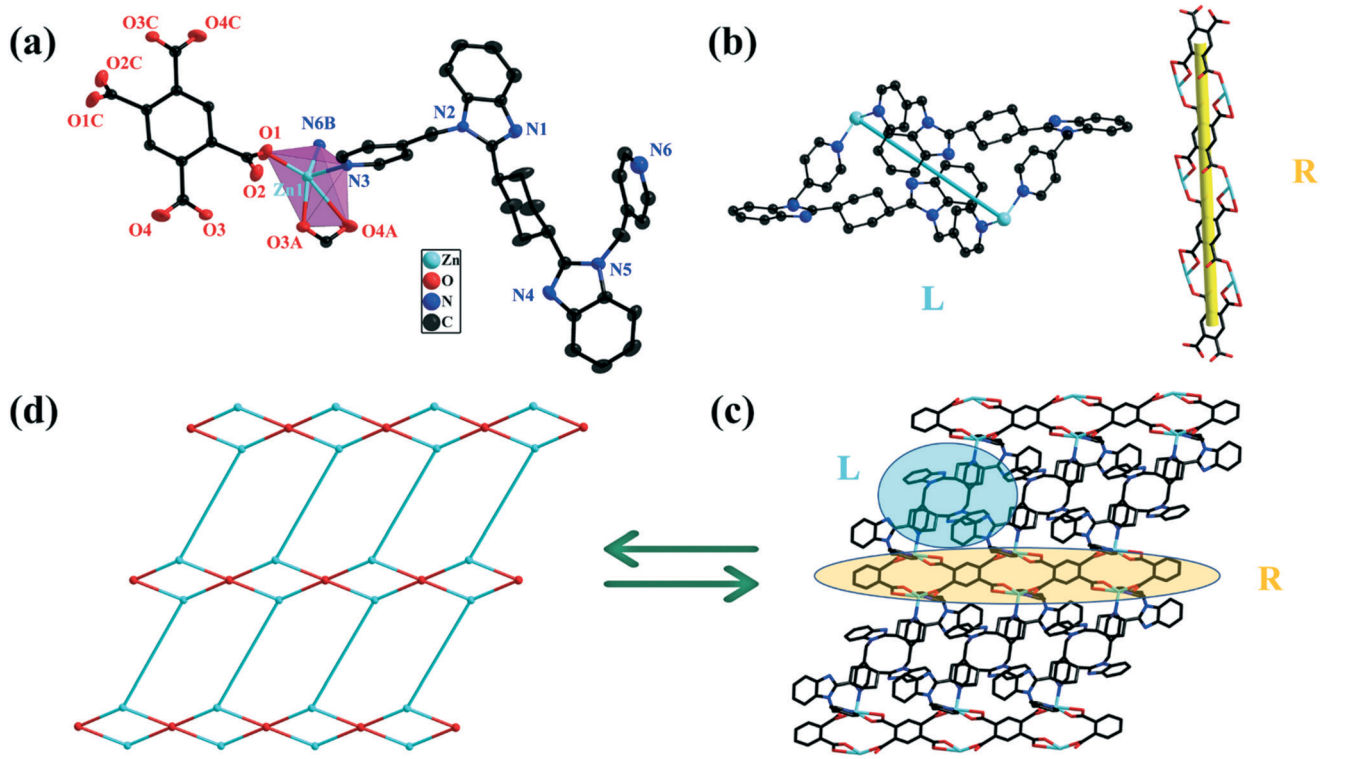

Fig. 1 (a) View of the coordination environment of Zn^{II} in MOF **1** with the ellipsoids drawn at the 30% probability level (H atoms omitted for clarity, symmetry code: symmetry code: A: 3 − *x*, 2 − *y*, −*z*, B: 2 − *x*, 1 − *y*, 1 − *z*.); (b) in MOF **1**, the $BTEC^{4-}$ anions connect the adjacent Zn^{II} ions to form a one-dimensional 1D straight-like line structure, and a binuclear $[Zn_2(L1)_2]$ unit was formed by L1 ligands and Zn^{II} atoms; (c) view of the complicated 2D framework with a 2D flat layer and $[Zn_2(L1)_2]$ unit in MOF **1**; (d) the **3,4L13** topological network of MOF **1** (cyan spheres: Zn^{II}; red spheres: $BTEC^{4-}$ anions; cyan sticks: $[Zn_2(L1)_2]$ ring).

The $BTEC^{4-}$ anions in **3** adopt two different μ_4-bridging modes, one where the four carboxylate groups are in a $(\kappa^1\text{-}\kappa^0)\text{-}(\kappa^1\text{-}\kappa^0)\text{-}(\kappa^1\text{-}\kappa^0)\text{-}(\kappa^1\text{-}\kappa^0)\text{-}\mu_4$ monodentate mode, and the other shows a $(\kappa^1\text{-}\kappa^0)\text{-}(\kappa^1\text{-}\kappa^1)\text{-}(\kappa^1\text{-}\kappa^0)\text{-}(\kappa^1\text{-}\kappa^1)\text{-}\mu_4$ mode. The $BTEC^{4-}$ anions connect the adjacent Zn(II) centers with two coordination modes to generate a $[Zn_4(BTEC)]_n$ 2D network (Fig. 2b). The L3 ligands adopt a *cis*-conformation mode with a $(\kappa^1)\text{-}(\kappa^1)\text{-}(\kappa^1)\text{-}(\kappa^0)\text{-}\mu_3$ mode to connect adjacent Zn(II) ions into a "Y"-like shape unit $[Zn_3(L3)]$. On the basis of these connection modes, the 2D $[Zn_4(BTEC)]_n$ networks are interconnected through the L3 ligands to extend the 2D layers into a 3D framework (Fig. 2c and S8a†). In order to simplify the structure of **3**, the Zn1 ions (cyan spheres) and two different $BTEC^{4-}$ anions (red spheres) can be regarded as 4-,4-,4-connected nodes, respectively. Zn2 ions (cyan spheres) and L3 ligands can be regarded as 3-,3-connected nodes, respectively. So the overall 3D network can be treated as an unprecedented (3,3,4,4,4)-connected 5-nodal network with a point symbol of $\{4\cdot8^2\}_2\{4^2\cdot6\cdot8^3\}_2\{4^2\cdot6\}_2\{4^2\cdot8^2\cdot10^2\}\{8^4\cdot12^2\}$ (Fig. 2d and S8b†).

Comparison of MOFs 1–4 and the influencing factors on their structural diversities

According to the crystal structure description of MOFs **1–4**, obviously, the coordination mode of $BTEC^{4-}$ anions is apparently very important for deciding the structural diversity of the MOFs. The $BTEC^{4-}$ anions are endowed with four carboxylate groups, which afford eight potential coordination sites and display versatile coordination modes for constructing new coordination polymers with interesting structures and specific topology (Chart 1). The detailed information of the coordination sites on $BTEC^{4-}$ anions is listed in Fig. 3. In MOFs **1** and **2**, the $BTEC^{4-}$ anions display a $(\kappa^1\text{-}\kappa^0)\text{-}(\kappa^1\text{-}\kappa^1)\text{-}(\kappa^1\text{-}\kappa^0)\text{-}(\kappa^1\text{-}\kappa^1)\text{-}\mu_4$ and $(\kappa^1\text{-}\kappa^0)\text{-}(\kappa^1\text{-}\kappa^0)\text{-}(\kappa^1\text{-}\kappa^0)\text{-}(\kappa^1\text{-}\kappa^0)\text{-}\mu_4$ mode, respectively, in which the carboxylate groups take part in the coordination to Zn(II) ions to form a 1D straight chain. However, the $BTEC^{4-}$ anions show a $(\kappa^1\text{-}\kappa^0)\text{-}(\kappa^1\text{-}\kappa^0)\text{-}(\kappa^1\text{-}\kappa^0)\text{-}(\kappa^1\text{-}\kappa^0)\text{-}\mu_4$ and $(\kappa^1\text{-}\kappa^0)\text{-}(\kappa^1\text{-}\kappa^1)\text{-}(\kappa^1\text{-}\kappa^0)\text{-}(\kappa^1\text{-}\kappa^1)\text{-}\mu_4$ coordination mode in MOF **3**, and two unequal $(\kappa^1\text{-}\kappa^1)\text{-}(\kappa^1\text{-}\kappa^1)\text{-}(\kappa^1\text{-}\kappa^1)\text{-}(\kappa^1\text{-}\kappa^1)\text{-}\mu_6$ coordination modes in MOF **4**, respectively, in which the carboxylate groups take part in the coordination to Zn(II) ions to form a 2D network. Besides that, auxiliary N-donor ligands also play a definite role in deciding the structural diversities of MOFs **1–4**, the auxiliary N-donor ligands have the same coordination number and the same configuration in MOFs **1–4** (all *trans*-conformation), and the only difference is their actual coordination mode with the metal Zn^{2+} center (Fig. S10†). In MOFs **1** and **2**, L1 and L2 ligands behave as a $(\kappa^0)\text{-}(\kappa^1)\text{-}(\kappa^0)\text{-}(\kappa^1)\text{-}\mu_2$ and $(\kappa^1)\text{-}(\kappa^1)\text{-}(\kappa^1)\text{-}(\kappa^0)\text{-}\mu_3$ mode, respectively. In the process of constructing the final structure, L2 can be regarded as a 4-connected node, while L1 can only be regarded as a linker. Therefore, the final structure

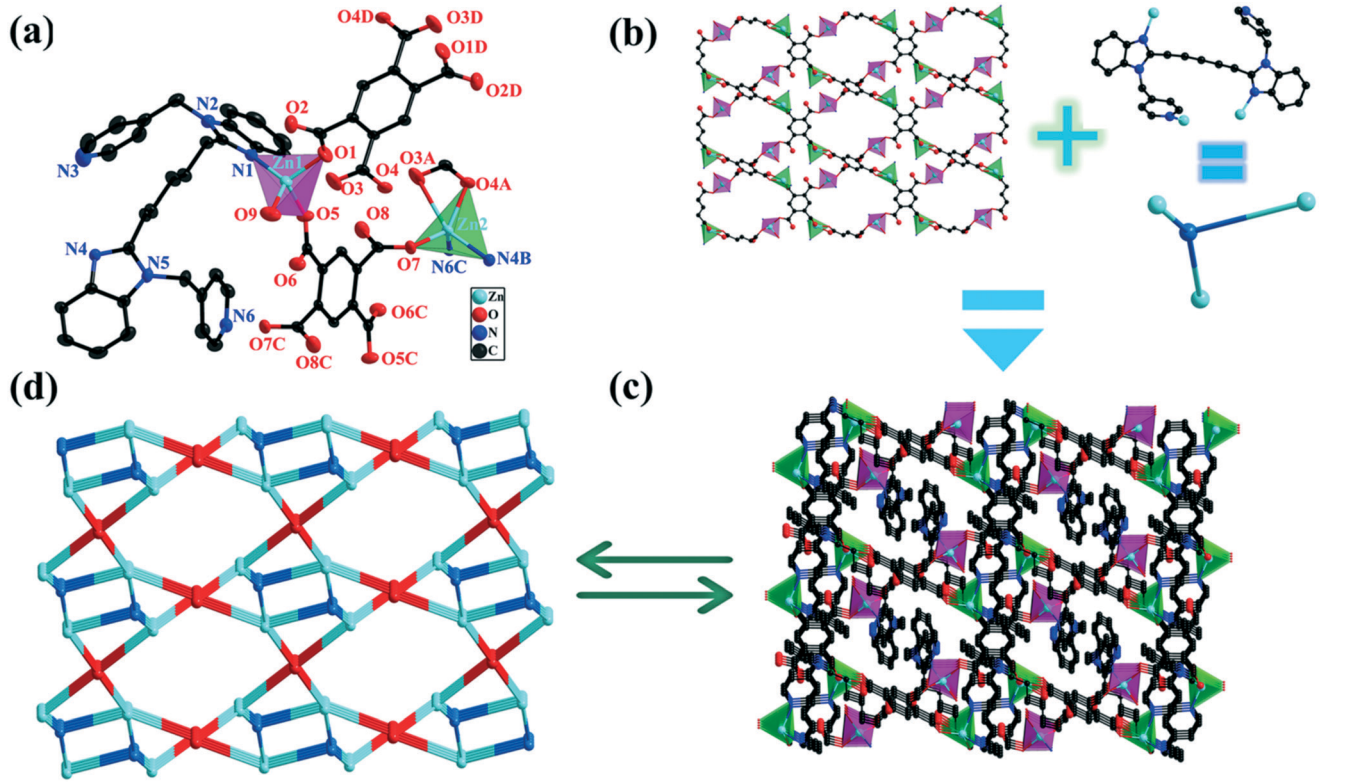

Fig. 2 (a) View of the coordination environment of Zn^{II} in MOF **3** with the ellipsoids drawn at the 30% probability level (H atoms are omitted for clarity, symmetry code: A: 1 + *x*, *y*, *z*; B: 1 + *x*, 1 + *y*, *z*; C: 2 − *x*, 1 − *y*, 1 − *z*; D: 1 − *x*, 1 − *y*, −*z*); (b) one varying 2D network, named as $[Zn_4(BTEC)_2]_n$, is formed by $BTEC^{4-}$ anions and Zn^{II} atoms in MOF **3** and one $[Zn_2(L3)_2]$ unit with the surrounding Zn^{II} atoms in MOF **3**; (c) a 3D layer structure formed by $[Zn_2(L3)_2]$ units and $[Zn_4(BTEC)_2]_n$ network; (d) a 3D structure with an unprecedented topology in MOF **3** (cyan spheres: Zn^{II} atoms; red spheres: $BTEC^{4-}$ anions; blue spheres: L3 ligands).

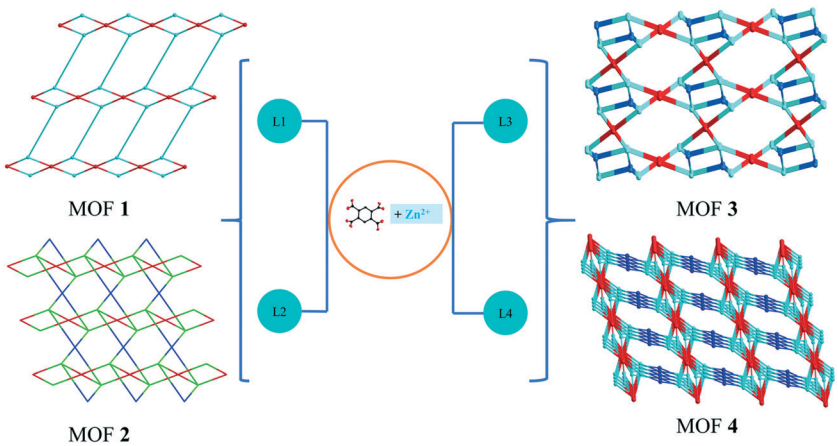

Chart 1 Schematic of the effect of the $BTEC^{4-}$ anion and L1–L4 ligands on the structures.

of MOF **1** can be regarded as a 3,4-connected **3,4L13** network, while **2** can be regarded as a 4,4,4-connected **4,4,4L10** network. In MOFs **3** and **4**, L3 and L4 ligands behave as a (κ^1)-(κ^1)-(κ^0)-(κ^1)-μ_2 and (κ^1)-(κ^1)-(κ^1)-(κ^1)-μ_4 mode, respectively. They can be regarded as a 3-connected node and 4-connected node, due to the slight difference between the coordination mode of $BTEC^{4-}$ anions and nitrogen-containing ligands, the final structures of MOFs **3** and **4** show distinct frameworks, where MOF **3** is a (3,3,4,4,4) connected 5-node network, and MOF **4** is a (4,4,4,6,6)-connected 5-node network.

Luminescence properties

Zn(II)-Based MOFs are of considerable concern because of their exceptional luminescence properties. On the other hand, benzimidazole and its derivatives are typical

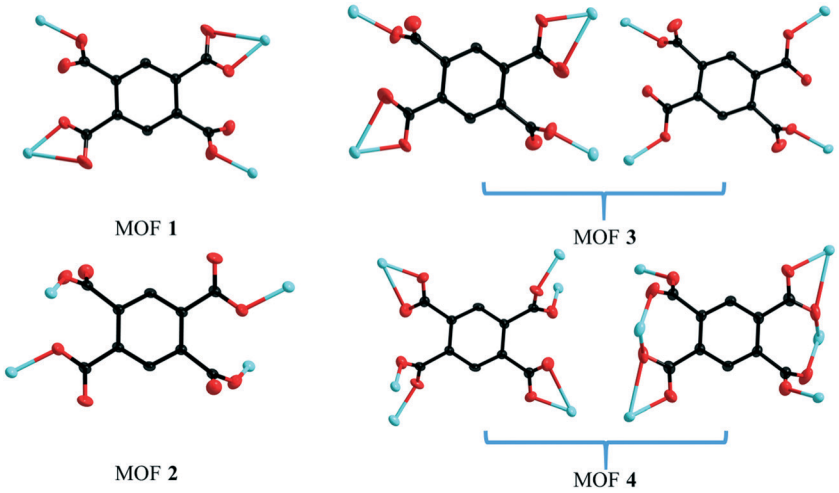

Fig. 3 View of the coordination modes of $BETC^{4-}$ anions in MOFs **1–4**.

heterocyclic ligands of nitrogen that contain charge transitions of $\pi \rightarrow \pi^*$,[46] where MOFs with L1–L4 may exhibit excellent optical properties. Thus, the solid-state luminescence spectra of MOFs **1–4**, free L1–L4 and H_4BTEC ligands were obtained at room temperature (Fig. 4 and S11†). The free L1–L4 and H_4BTEC ligands present emission bands at 318 nm (λ_{ex} = 328 nm), 302 nm (λ_{ex} = 310 nm), 301 nm (λ_{ex} = 333 nm), 304 nm (λ_{ex} = 372 nm), and 351 nm (λ_{ex} = 298 nm), respectively. MOFs **1–4** reveal emission maxima at 396 nm (λ_{ex} = 301 nm), 403 nm (λ_{ex} = 289 nm), 386 nm (λ_{ex} = 305 nm), and 411 nm (λ_{ex} = 311 nm), respectively. The spectra of MOFs **1–4** highly resemble those of H_4BTEC ligands, which implies that the luminescence of MOFs **1–4** comes from H_4-BTEC ligands. The energy transfer may take place from the L1–L4 ligands to dicarboxylate ligands. MOFs **1–4** show red-shifts compared with the corresponding ligands, which may stem from the coordination effects of ligands to Zn(II) centers.[47,48] As Zn(II) ions are not readily oxidized or reduced, they are necessarily neither MLCT nor LMCT. The emission spectra of MOFs **1–4** can emerge from the transition of intra-ligand charge and LLCT mixtures; the lower the energy of the LUMO of H_4BTEC ligands than that of the L1–L4 ligands, the higher the probability of electron transfer from the L1–L4 ligands to H_4BTEC ligands[49,50] (Table S5†).

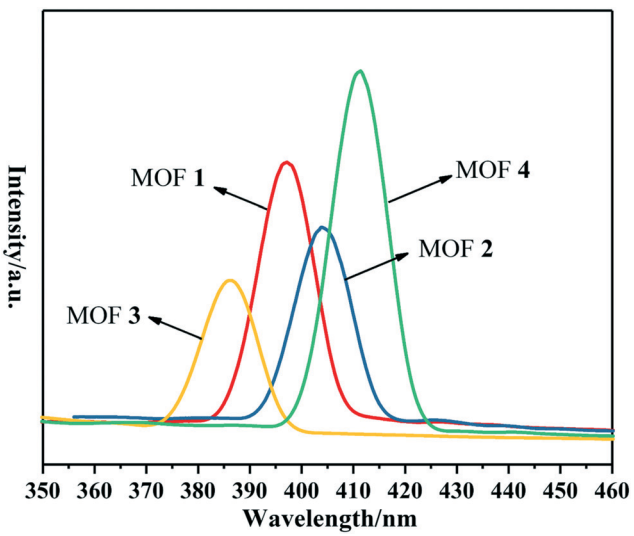

Fig. 4 Solid-state emission spectra of MOFs **1–4** at room temperature.

Acetylacetone sensing

An ethanol suspension of MOFs **1–4** was used for fluorescence detection of various small organic molecules. Since MOFs **1–4** contain ethanol molecules and exhibit strong solution stability, ethanol is selected as the dispersion medium. The fluorescence emission intensities of MOFs **1–4** depend on various solvents; in particular, acetylacetone (acac) shows an apparent fluorescence quenching operation, while other solvents only have mild fluorescence enhancement or fluorescence quenching (Fig. 5a and S12a–S14a†). Notably, it exhibits the most remarkable turn-off fluorescence after the addition of acac. The visual emission color of the suspension of MOFs **1–4** with 7.6 μmol L^{-1} acac changed from blue to light blue when excited at 365 nm with a UV lamp (insert of Fig. 5). For this reason, MOFs **1–4** can be used as fluorescent samples to detect acac. Anti-interference tests were recorded with the inclusion of MOFs **1–4** equiv. of other organics in view of the high selectivity of MOFs **1–4** toward acac. The results demonstrate that the other solvents barely impact the fluorescence emission rate of MOFs **1–4** in the absence of acac. However, the emission intensity of MOFs **1–4** is totally quenched by the addition of acac to the above solution (Fig. 5b and S12b–S14b). These findings suggest that compared to other solvents, MOFs **1–4** are highly sensitive against acac. The time-dependent fluorescence emission response spectra were also further measured. After adding acac with a concentration of 7.6 μmol L^{-1} over 30 s, the emission intensities of MOFs **1–4** decrease significantly, which demonstrates that MOFs **1–4** could be used as probes with high sensitivity to detect acac (Fig. S15†).

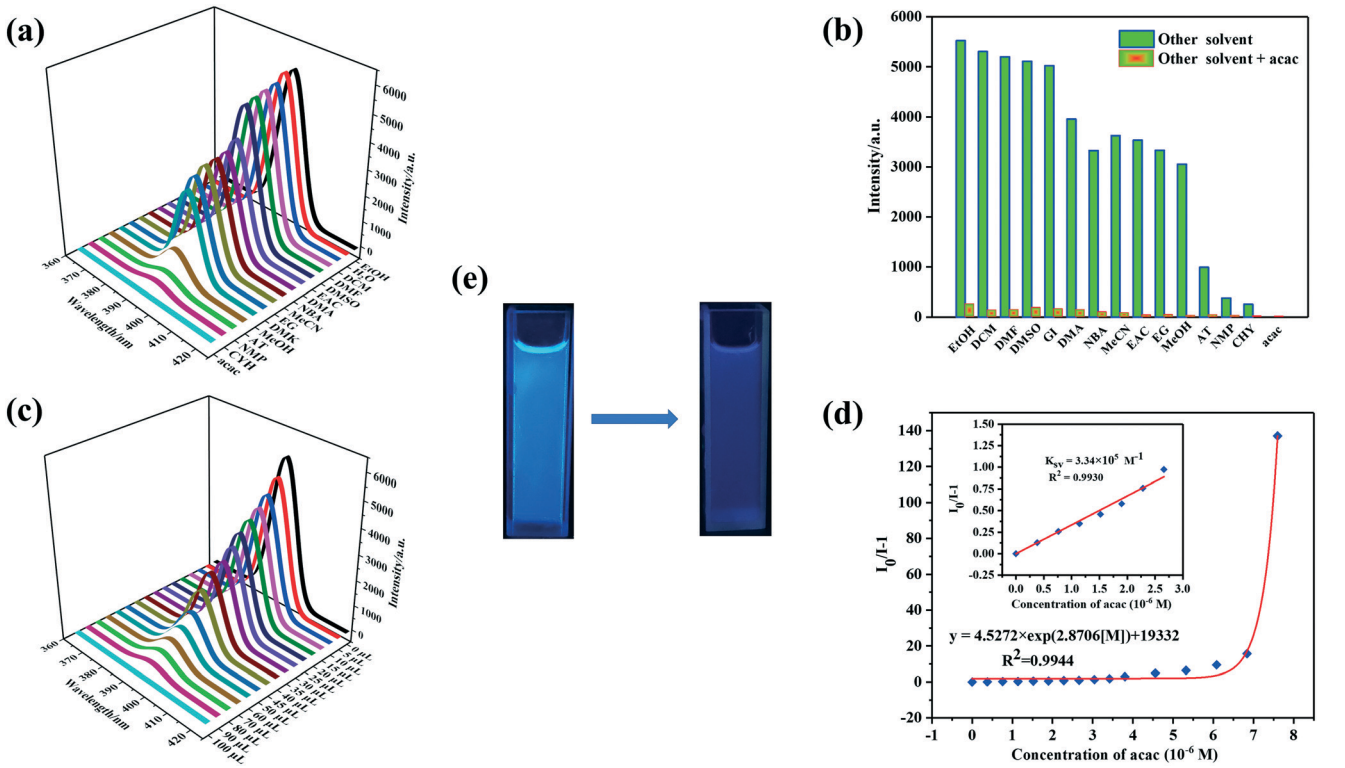

Fig. 5 (a) Photoluminescence intensities of MOF **1** introduced into organic solvents at room temperature, λ_{ex} = 301 nm; (b) influence of interfering organic solvents on the luminescence intensity of acac at room temperature in MOF **1**, λ_{ex} = 301 nm; (c) fluorescence emission intensity at different concentrations (0–100 μL, the corresponding concentrations are 0–7.6 μmol L^{-1}) of acac using H_2O as the solvent in MOF **1**, λ_{ex} = 301 nm; (d) relationship between $I_0/I - 1$ and different concentrations of acac (I_0 and I refer to the luminescence intensity of MOF **1** without and with acac, respectively). Insert: Linear plot of $I_0/I - 1$ and low acac concentration of MOF **1**; (e) the changes in the fluorescence images of the aqueous dispersion of the MOF **1** before and after quenching titration.

Further experiments on the relationship between luminescence changes of MOFs **1–4** and the concentration acac (0–100 μL, the corresponding concentrations are 0–7.6 μmol L^{-1}) were also discussed in depth. The curve shows that the related luminescence strength changes of MOFs **1–4** could be clearly detected and the quenching results were exceptional at the same time, demonstrating an exemplary sensitivity to acac sensing (Fig. 5c and S12c–S14c†). The diminished luminescence intensity of MOFs **1–4** with increasing acac meant that the luminescence quenching effect of MOFs **1–4** was present. The relationship between the quenching efficiency of MOFs **1–4** and the concentration of acac is shown in Fig. 5d and S12d–S14d.† As a result, the best fit of I_0/I *vs.* the concentration of acac was established with a first-order exponential decay formula of $I_0/I = K_{SV}[acac] + 1$, where K_{SV} represents the quenching constant (M^{-1}), I_0 and I are the luminescence intensities before and after the addition of acetylacetone, and [acac] is the molar concentration of acetylacetone, respectively.[51] The outcome shows a linear association between luminescence quenching and acac concentration (0–2.66 μmol L^{-1}) which is similar to the Stern–Volmer (SV) equation.[52] The average K_{SV} value obtained by linear regression of the plot was determined to be 3.34 × 10^5 M^{-1}, 2.06 × 10^5 M^{-1}, 2.44 × 10^5 M^{-1} and 2.89 × 10^5 M^{-1}, suggesting a substantial quenching efficiency of MOFs **1–4** after the addition of acac. acac identification limits can be determined by using $3\delta/k$,[53] in which δ is a normal error and k is the slope according to the Stern–Volmer equation with a value of 0.101, 0.165, 0.193 and 0.138 μM L^{-1} for MOFs **1–4**, respectively, which is comparable with that of reported probes for sensing of acetylacetone and further indicative of excellent sensitivity for sensing acac[7–12] (Table 1).

Selective detection of Fe^{3+} ions

In various metal nitrate solutions, the fluorescence emission spectra of MOFs **1–4** indicate various degrees of quenching for different cations (Fig. 6a and S16a–S18a†). Only Fe^{3+} ions display a strong fluorescence quenching effect, while other transition metal cations and high valent cations have demonstrated limited quenching or enhancement effects. The visual emission color of the suspension of MOFs **1–4** with 6 × 10^{-3} M acac changed from blue to light blue when excited at 365 nm with a UV lamp (insert of Fig. 6). In addition, by adding Fe^{3+} ions, and concurrently some other different metal cations, the intensities of the emission spectra of MOFs **1–4** scattered in water suspensions were also compared, showing that MOFs **1–4** have extremely selective discrimination in

Table 1 Comparison of the sensitivities of MOFs **1–4** with previously reported MOFs to acac

MOF	Types	LOD/M	Ref.
$\{[Zn_3(bbib)_2(ndc)_3]\cdot 2DMF\cdot 2H_2O\}_n$	acac	0.100×10^{-6}	7
$\{[(CH_3)_2NH_2][Zn(FDA)(BTZ)_2]\}_n$	acac	0.647×10^{-6}	8
$\{[Zn_2(XN)_2(IPA)_2]\cdot 2H_2O\}_n$	acac	0.25×10^{-6}	9
$\{[Zn(XL)_2](ClO_4)_2\cdot 6H_2O\}_n$	acac	1.72×10^{-6}	10
$\{[Cd(L)(1,4\text{-PDA})]\cdot 0.7(C_2H_5OH)\}_n$	acac	2.45×10^{-6}	11
$\{[Cd(L)_{0.5}(1,8\text{-NDC})\cdot H_2O]\}_n$	acac	1.40×10^{-6}	11
$[Cd_2(L2)_2(DCTP)_2]_n$	acac	0.636×10^{-6}	12
$\{[Cd_2(L3)(DCTP)_2]\cdot 3.75H_2O\}_n$	acac	0.876×10^{-6}	12
MOF **1**	acac	0.101×10^{-6}	This work
MOF **2**	acac	0.165×10^{-6}	This work
MOF **3**	acac	0.193×10^{-6}	This work
MOF **4**	acac	0.138×10^{-6}	This work

bbib = 1,3-bis(benzimidazolyl)benzene, and H_2ndc = 1,4naphthalenedicarboxylic acid; H_2FDA = furan 2,5-dicarboxylic acid, and HBTZ = 1*H*-benzotriazole; XN = 4′-(4-pyridine)4,2′:2′,4″-terpyridine, and IPA = isophthalic acid; XL = *N*,*N*′-bicyclo[2.2.2]oct-7-ene2,3,5,6-tetracarboxdiimide bi(1,2,4-triazole); L = 1,4-bis(5,6-dimethybenzimidazol-1-yl)-2-butene, 1,4-H_2PDA = 1.4-phenylenediacetic acid, 1,8-H_2NDC = 1,8-naphthalenedicarboxylic acid; L2 = 1,5-di(1*H*-benzo[*d*]imidazol-2-yl)pentane, L3 = 1,3-bis(1-(pyridin-4-ylmethyl)-1*H*-benzo[*d*]imidazol-2-yl) propane, and H_2DCTP = 2,5-dichloroterephthalic acid.

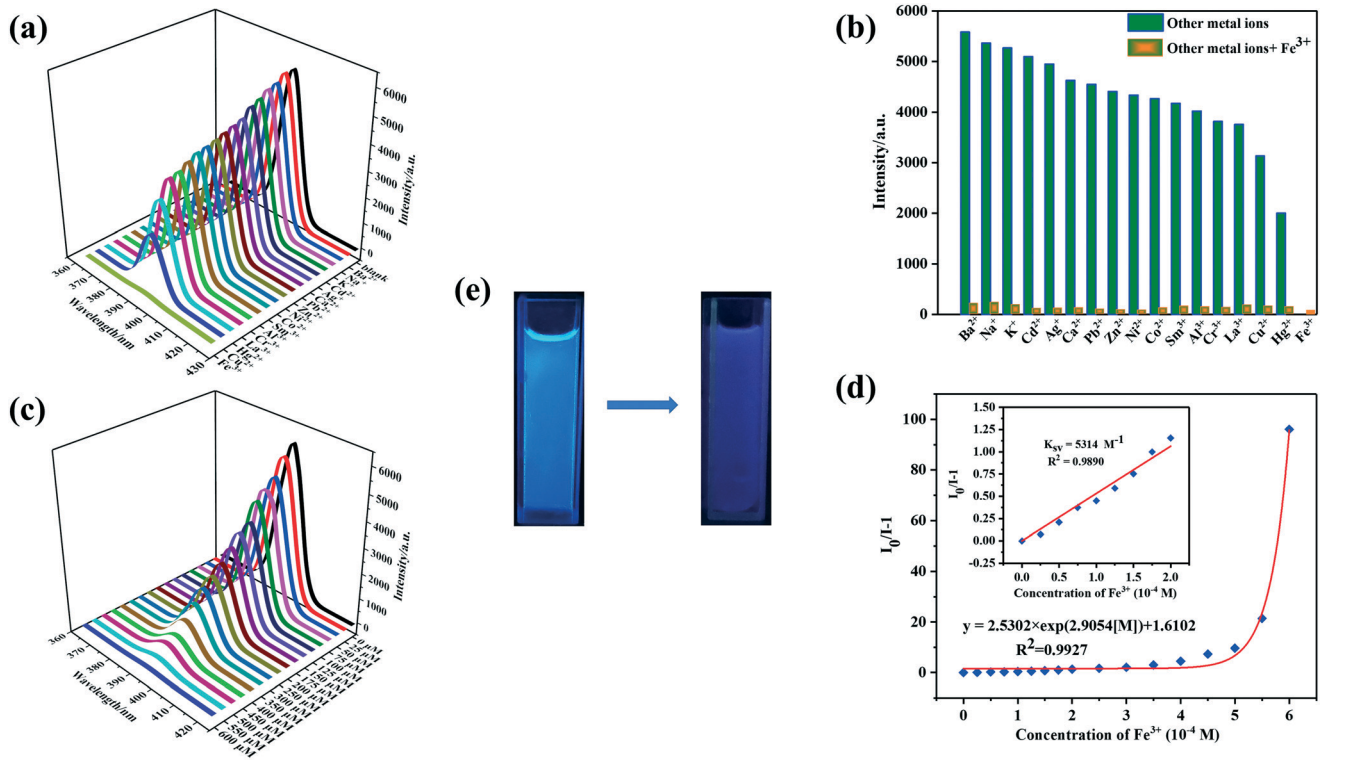

Fig. 6 (a) Luminescence spectra of MOF **1** with different metal ions (10^{-4} M) in EtOH/H_2O (1 : 1, v/v) solutions at 301 nm. (b) Influence of interfering ions on the luminescence intensity of Fe^{3+} ions at room temperature in EtOH/H_2O (1 : 1, v/v) solutions, λ_{ex} = 301 nm. (c) Liquid emission spectra of MOF **1** as a result of different concentrations of Fe^{3+} ions at room temperature in EtOH/H_2O (1 : 1, v/v) solutions, λ_{ex} = 301 nm. (d) Plot of relative intensity *vs.* Fe^{3+} ion concentration; (e) the changes in the fluorescence images of the EtOH/H_2O dispersion of the MOF **1** before and after quenching titration.

aqueous solutions of Fe^{3+} ions (Fig. 6b and S16b–S18b†). Using 0.4 ml of Fe^{3+} ions (10^{-3} M), the fluorescence emission reaction was further determined over time. The fluorescence emission was substantially decreased after 30 s, indicating that the aqueous solution of MOFs **1–4** was chemically sensitive to Fe^{3+} ions (Fig. S19†). For highly selective and sensitive Fe^{3+} ion luminescence detection, these MOFs may be used as perfect fluorescence monitoring probe materials.

To help comprehend the sensitivities of MOFs **1–4** to Fe^{3+} ion fluorescence detection, quantitative luminescence titration tests of MOFs **1–4** were also conducted by applying various Fe^{3+} ion concentrations ranging from 0 to 6×10^{-3} M

to the suspension. The fluorescence intensity of the suspensions of MOFs **1–4** steadily decreased with the rise in the Fe^{3+} ion concentration (Fig. 6c and S16c–S18c†). Generally, the kinetics of Stern–Volmer (SV) were used to account for static fluorescence intensity quenching to describe the relationship between the Fe^{3+} ion concentration and the effects of quenching (Fig. 6d and S16d–S18d†),[54] which can be adapted using the $K_{SV} = [I_0/I - 1]/[M]$, where I and I_0 are the fluorescence intensities in the presence or absence of Fe^{3+} ions, respectively; K_{SV} is the Stern–Volmer constant; and [M] represents the concentration of Fe^{3+} ions. At low concentrations stages, the curves of $[I_0/I - 1]$ *versus* Fe^{3+} ion concentration display a compliant linear association, which is primarily due to static quenching.[55] The K_{SV} values of MOFs **1–4** are expected to be 5314 M^{-1}, 6775 M^{-1}, 6636 M^{-1} and 6424 M^{-1}; the limit of detection (LOD) is very low, exceeding 6.35, 5.01, 7.02 and 6.19 μM, respectively, indicating that MOFs **1–4** have high efficiency of luminescence quenching for Fe^{3+} ions. Compared with other MOF fluorescence probes that detect Fe^{3+} ions, the sensitivity of MOFs **1–4** is equivalent or superior (Table 2).[1–4,6,21,24]

Post-processing and chemical stability analysis

To further identify the recognition sites on the MOFs for acac and Fe^{3+} ions, under the same conditions as the MOF **1** experiment, fluorescence recognition experiments toward acac/Fe^{3+} of L1 and H_4BTEC ligands were carried out (Fig. S20 and S21†). The results show that L1 and H_4BTEC ligands have a slight quenching effect on acac and Fe^{3+} ions, and the quenching efficiencies are 62.10/66.06% (acac/Fe^{3+} ions) and 76.24/59.09%, respectively. As a result, H_4BTEC and L1 ligands had slight fluorescence while MOFs **1–4** had obvious fluorescence. All the above results could confirm that the luminescence was caused by the MOFs, not the decomposition of crystalline structures.

To verify the recyclability of MOFs **1–4** for acac and Fe^{3+} testing, a reversible processing experiment was performed. Powder MOFs **1–4** were immersed in acac and Fe^{3+} ion anion solutions for 24 h, then washed and recovered for fluorescence detection. After four detection cycles, the quenching effect of recovered MOFs **1–4** on acac/Fe^{3+} was still obviously observed (Fig. S22†). After the cyclic test, the PXRD spectra of MOFs **1–4** were compatible with those of the originally synthesized ones, meaning that the repeatability of MOFs **1–4** was excellent (Fig. S23†). The fluorescence intensity of MOFs **1–4** was measured during sensing of acac/Fe^{3+} by adjusting the pH values (Fig. S24†). During detection of Fe^{3+} ions (pH = 4–8) and acac (pH = 4–10), the fluorescence intensity fluctuations of MOFs **1–4** show little change. To further disclose their interior nature, transmission electron microscopy (TEM) images were obtained, which suggested that MOFs **1–4** have a nanopore structure (100 nm) (Fig. 7a and S25a–S27a†).[56] Furthermore, the typical EDX elemental mapping image of a particle of MOFs **1–4** reveals the co-existence and homogeneous distribution of the elements C, N, O, Zn, and Fe after detecting Fe^{3+} ions (Fig. 7b and S25b–S27b†). Therefore, these MOFs could behave as luminescent probes for Fe^{3+} ions/acac with high selectivity and sensitivity.

Mechanism of luminescence quenching

To further confirm the high selectivity of MOFs **1–4** for the detection of Fe^{3+} ions and acetylacetone we studied the luminescence quenching mechanism. After three cycles of tests, the consistency between the PXRD patterns and the initial patterns is very high, which makes it clear that the composition of MOFs **1–4** did not change during the

Table 2 Comparison of the sensitivities of MOFs **1–4** with previously reported MOFs to Fe^{3+} ions

MOF	Types	LOD/M	Ref.
$\{[Zn_2(\mu_4\text{-L})(\mu\text{-mbix})_2]\cdot 2H_2O\}_n$	Fe^{3+}	3.23×10^{-6}	1
$\{[Zn_3(HL)_2H_2O]\cdot 4H_2O\}_n$	Fe^{3+}	2.2×10^{-4}	2
$\{[Zn(L)(dcdps)]\}_n$	Fe^{3+}	6.21×10^{-5}	3
$\{Zn(L)(bdc)\}_n$	Fe^{3+}	4.45×10^{-5}	3
$\{[Cd(L)(oba)]\cdot 0.5DMF\}_n$	Fe^{3+}	11.52×10^{-5}	3
$\{[Cd(L)(bdc)\cdot 2H_2O]\cdot 2DMF\}_n$	Fe^{3+}	6.36×10^{-5}	3
$[Cd_2(TB)(H_2O)_4]\cdot 3DMF\cdot H_2O$	Fe^{3+}	1.1×10^{-5}	4
$[Zn(TIBTC)(DMA)]\cdot[NH_2(CH_3)_2]$	Fe^{3+}	3.45×10^{-6}	6
$[Cd(TIBTC)(H_2O)]\cdot[NH_2(CH_3)_2]\cdot DMA$	Fe^{3+}	5.51×10^{-6}	6
$[Zn_3(L)_2(4,4'\text{-bbibp})_2(H_2O)_2]_n\cdot 2(CH_3CN)$	Fe^{3+}	0.35×10^{-6}	24
$\{[Co_3(BIBT)_3(BTC)_2(H_2O)_2]\cdot solvents\}_n$	Fe^{3+}	0.13×10^{-6}	21
$[Zn_2(chtc)(H_2O)]\cdot 3H_2O$	Fe^{3+}	3.5×10^{-6}	20
MOF **1**	Fe^{3+}	6.35×10^{-6}	This work
MOF **2**	Fe^{3+}	5.01×10^{-6}	This work
MOF **3**	Fe^{3+}	7.02×10^{-6}	This work
MOF **4**	Fe^{3+}	6.19×10^{-6}	This work

H_4L = (*E*)-5,5′-(but2-ene-1,4-diylbis(oxy))diisophthalic acid, mbix = 1,3-bis((imidazol-1-yl)methyl)benzene; H_4L = 1-(3,5-dicarboxylatobenzyl)-3,5-pyrazole dicarboxylic acid; L = 4,4′-(2,5-bis(methylthio)-1,4-phenylene)dipyridine; H_2dcdps = 4,4′-sulfonyldibenzoic acid, H_2bdc = 1,4-dicarboxybenzene, H_2oba = 4,4′oxybisbenzoic acid; H_4TB = 3,3′,5,5′-tetra(4-carboxyphenyl)bimesityl; H_3TIBTC = 2,4,6-triiodo-1,3,5-benzenetricarboxylic acid; H_3L = 5-(2-carboxylphenoxy)isophthalic acid, semi-flexible 1,4-bimb = 1,4-bis(imidazol-l-ylmethyl) benzene; H_2chtc = deprotonate/half-protonate cyclohexane-1*e*,2*a*,4*a*,5*e*-tetracarboxylic acid.

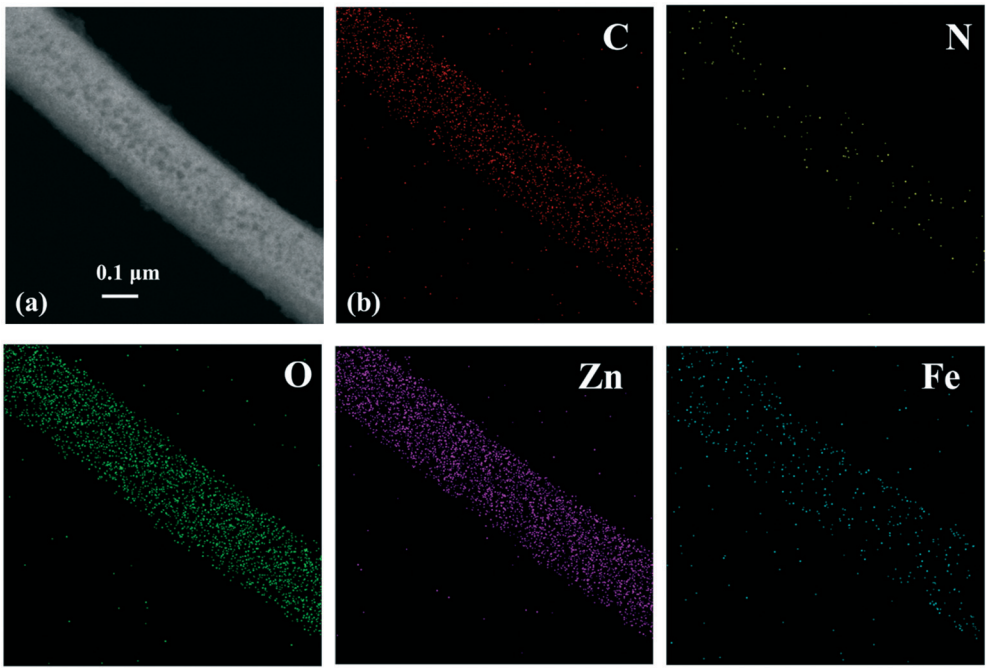

Fig. 7 (a) TEM image of MOF **1**; (b) TEM elemental mapping images of C, O, N, Zn and Fe after detecting Fe^{3+} ions.

detection process (Fig. S23†). Then density functional theory (DFT) calculations were performed on MOFs **1–4** and Fe^{3+} ions/acac molecules (Fig. S28, Table S5†). Undoubtedly, the lower the energy of the LUMO of an analyte than that of the MOF, the higher the probability of electron transfer from the MOF to the analyte. The excited electrons in the LUMO of MOFs **1–4** generated under the excitation of photons are transferred to the LUMO of Fe^{3+} ions/acac, thereby weakening the fluorescence of MOFs **1–4**. Accordingly, a photo-induced electron transfer mechanism is assumed.[57,58] However, the nonlinear trend of the electron transfer cannot be the sole cause of luminescence quenching. Therefore, a resonance energy-transfer mechanism was taken into consideration.[59,60] Although the suggested resonance energy transfer mechanism involves a spectral overlap between the donor and the acceptor, we analyzed the UV-vis absorption of Fe^{3+} ions/acetylacetone and other tested analytes in order to further support this mechanism (Fig. S29 and S30†). Only the UV-vis absorption band of Fe^{3+} ions/acetylacetone (starting at 250 nm and ending at 370 nm) overlaps with the excitation peaks of MOFs **1–4** (270–340 nm), making it possible to transfer resonance energy in Fe^{3+} ion/acetylacetone sensing systems. The comparisons above demonstrate the proposed quenching process and also describe the selectivity of the response to Fe^{3+} ions/acetylacetone in MOFs **1–4**.[61]

Conclusion

In summary, under hydrothermal conditions, four new MOFs with distinct bis(benzimidazole) and $BETC^{4-}$ ligands have been synthesized. The coordination modes of $BETC^{4-}$ anions and N-donor ligands have a major influence on the development of these various topological structures in the self-assembly process. Furthermore, MOFs **1–4** display excellent selective and sensitive abilities with low detection limits and good recyclability as luminescent sensors for detection of Fe^{3+}/acetylacetone.

Conflicts of interest

The authors have declared no conflict of interest.

Acknowledgements

This project was supported by the National Natural Science Foundation of China (51474086).

References

1 M. Arıcı, Y. C. Dikilitaş, H. Erer and O. Z. Yeşilel, *CrystEngComm*, 2020, **22**, 5776–5785.
2 W. N. Liu, W. Q. Tong, L. L. Ma, Y. Wang, J. M. Wang, L. Hou and Y. Y. Wang, *Dalton Trans.*, 2019, **48**, 7786–7793.
3 F. Y. Ge, G. H. Sun, L. Meng, S. S. Ren and H. G. Zheng, *Cryst. Growth Des.*, 2019, **20**, 1898–1904.
4 X. Wang, W. Fan, M. Zhang, Y. Shang, Y. Wang, D. Liu, H. Guo, F. Dai and D. Sun, *Chin. Chem. Lett.*, 2019, **30**, 801–805.
5 S. Sen, M. H. Al-Sayah, M. S. Mohammed, I. I. Abu-Abdoun and O. M. El-Kadri, *J. Mater. Sci.*, 2020, **55**, 10896–10909.
6 C. H. Liu, Q. L. Guan, X. D. Yang, F. Y. Bai, L. X. Sun and Y. H. Xing, *Inorg. Chem.*, 2020, **59**, 8081–8098.
7 S. L. Yao, S. J. Liu, X. M. Tian, T. F. Zheng, C. Cao, C. Y. Niu, Y. Q. Chen, J. L. Chen, H. Huang and H. R. Wen, *Inorg. Chem.*, 2019, **58**, 3578–3581.
8 J. Y. Zou, L. Li, S. Y. You, K. H. Chen, X. N. Dong, Y. H. Chen and J. Z. Cui, *Cryst. Growth Des.*, 2018, **18**, 3997–4003.

9 X. M. Kang, X. Y. Fan, P. Y. Hao, W. M. Wang and B. Zhao, *Inorg. Chem. Front.*, 2019, **6**, 271–277.
10 X. M. Kang, R. R. Cheng, H. Xu, W. M. Wang and B. Zhao, *Chemistry*, 2017, **23**, 13289–13293.
11 Y. S. Shi, Y. H. Li, G. H. Cui and G. Y. Dong, *CrystEngComm*, 2020, **22**, 905–914.
12 Y. S. Shi, D. Liu, L. Fu, Y. Li and G. Dong, *CrystEngComm*, 2020, **22**, 4079–4093.
13 M. Singh, S. Senthilkumar, S. Rajput and S. Neogi, *Inorg. Chem.*, 2020, **59**, 3012–3025.
14 S. Venkateswarlu, A. S. Reddy, A. Panda, D. Sarkar, Y. Son and M. Yoon, *ACS Appl. Nano Mater.*, 2020, **3**, 3684–3692.
15 C. Xia, Y. Xu, M. M. Cao, Y. P. Liu, J. F. Xia, D. Y. Jiang, G. H. Zhou, R. J. Xie, D. F. Zhang and H. L. Li, *Talanta*, 2020, **212**, 120795.
16 H. Tan, X. Wu, Y. Weng, Y. Lu and Z. Z. Huang, *Anal. Chem.*, 2020, **92**, 3447–3454.
17 M. Bagheri and M. Y. Masoomi, *ACS Appl. Mater. Interfaces*, 2020, **12**, 4625–4631.
18 T. Wiwasuku, J. Othong, J. Boonmak, V. Ervithayasuporn and S. Youngme, *Dalton Trans.*, 2020, **49**, 10240–10249.
19 A. Mukhopadhyay, S. Jindal, G. Savitha and J. N. Moorthy, *Inorg. Chem.*, 2020, **59**, 6202–6213.
20 M. T. Chen, X. D. Xie, J. X. Meng, Y. C. Ou, J. Z. Wu and M. L. Tong, *CrystEngComm*, 2020, **22**, 6713–6719.
21 X. M. Tian, S. L. Yao, C. Q. Qiu, T. F. Zheng, Y. Q. Chen, H. Huang, J. L. Chen, S. J. Liu and H. R. Wen, *Inorg. Chem.*, 2020, **59**, 2803–2810.
22 Z. Sun, J. Sun, L. Xi, J. Xie, X. Wang, Y. Ma and L. Li, *Cryst. Growth Des.*, 2020, **20**, 5225–5234.
23 L. Wang, B. Tu, W. Xu, Y. Fu and Y. Zheng, *Inorg. Chem.*, 2020, **59**, 5004–5017.
24 C. Fan, X. Zhang, N. Li, C. Xu, R. Wu, B. Zhu, G. Zhang, S. Bi and Y. Fan, *J. Pharm. Biomed. Anal.*, 2020, **188**, 113444.
25 Q. Q. Zhu, Q. S. Zhou, H. W. Zhang, W. W. Zhang, D. Q. Lu, M. T. Guo, Y. Yuan, F. Sun and H. He, *Inorg. Chem.*, 2020, **59**, 1323–1331.
26 Y. Mu, Y. Ran, B. Zhang, J. Du, C. Jiang and J. Du, *Cryst. Growth Des.*, 2020, **20**, 6030–6043.
27 L. Yu, Q. Zheng, H. Wang, C. Liu, X. Huang and Y. Xiao, *Anal. Chem.*, 2020, **92**, 1402–1408.
28 P. Li, N. A. Vermeulen, X. Gong, C. D. Malliakas, J. F. Stoddart, J. T. Hupp and O. K. Farha, *Angew. Chem., Int. Ed.*, 2016, **55**, 10358–10362.
29 A. J. Howarth, Y. Liu, P. Li, Z. Li, T. C. Wang, J. T. Hupp and O. K. Farha, *Nat. Rev. Mater.*, 2016, **1**, 15018.
30 X. Zhang, Z. Chen, X. Liu, S. L. Hanna, X. Wang, R. Taheri-Ledari, A. Maleki, P. Li and O. K. Farha, *Chem. Soc. Rev.*, 2020, **49**, 7406–7427.
31 J. X. Yang, X. Zhang, Y. Y. Qin and Y. G. Yao, *Cryst. Growth Des.*, 2020, **20**, 6366–6381.
32 J. Ma, N. Xu, Y. Liu, Y. Wang, H. Li, G. Liu, X. Wang and J. Li, *Inorg. Chem.*, 2020, **59**, 15495–15503.
33 M. A. Silva, N. R. de Campos, L. A. Ferreira, L. S. Flores, J. C. A. Júnior, G. L. dos Santos, C. C. Corrêa, T. C. dos Santos, C. M. Ronconi, M. V. Colaço, T. R. G. Simões, L. F. Marques and M. V. Marinho, *Inorg. Chim. Acta*, 2019, **495**, 118967.
34 Agilent, *CrysAlis PRO*, Agilent Technologies Ltd, Yarnton, Oxfordshire, England, 2014.
35 O. V. Dolomanov, L. J. Bourhis, R. J, J. A. K. Gildea, J. A. K. Howard and H. Puschmann, *J. Appl. Crystallogr.*, 2020, **42**, 339–341.
36 L. J. Bourhis, O. V. Dolomanov, R. J. Gildea, J. A. K. Howard and H. Puschmann, *Acta Crystallogr., Sect. A: Found. Adv.*, 2020, **71**, 59–75.
37 G. M. Sheldrick, *Acta Crystallogr., Sect. C: Struct. Chem.*, 2015, **71**, 3–8.
38 A. L. Spek, *Acta Crystallogr., Sect. D: Biol. Crystallogr.*, 2009, **65**, 148–155.
39 S. Y. Hao, S. X. Hou, Z. C. Hao and G. H. Cui, *Spectrochim. Acta, Part A*, 2018, **189**, 613–620.
40 S. Y. Hao, Y. H. Li, Z. C. Hao and G. H. Cui, *Ultrason. Sonochem.*, 2017, **39**, 636–644.
41 Y. Deng, Z. Y. Yao, P. Wang, Y. Zhao, Y. S. Kang and W. Y. Sun, *Sens. Actuators, B*, 2017, **244**, 114–123.
42 Y. Zhao, X. Xu, L. Qiu, X. Kang, L. Wen and B. Zhang, *ACS Appl. Mater. Interfaces*, 2017, **9**, 15164–15175.
43 Z. Q. Liu, Y. Zhao, X. D. Zhang, Y. S. Kang, Q. Y. Lu, M. Azam, S. I. Al-Resayes and W. Y. Sun, *Dalton Trans.*, 2017, **46**, 13943–13951.
44 V. A. Blatov, *Struct. Chem.*, 2012, **23**, 955–963.
45 B. Qin, X. Zhang and J. Zhang, *Cryst. Growth Des.*, 2020, **20**, 5120–5128.
46 J. Troyano, E. Zapata, J. Perles, P. Amo-Ochoa, V. Fernández-Moreira, J. I. Martínez, F. Zamora and S. Delgado, *Inorg. Chem.*, 2019, **58**, 3290–3301.
47 X. Zhou, Y. X. Shi, C. Cao, C. Y. Ni, Z. G. Ren, D. J. Young and J. P. Lang, *Cryst. Growth Des.*, 2019, **19**, 3518–3528.
48 G. Liu, S. Han, Y. Gao, N. Xu, X. Wang and B. Chen, *CrystEngComm*, 2020, **22**, 7952–7961.
49 J. A. Hua, Y. Zhao, Y. S. Kang, Y. Lu and W. Y. Sun, *Dalton Trans.*, 2015, **44**, 11524–11532.
50 Y. Rachuri, B. Parmar, K. K. Bisht and E. Suresh, *Dalton Trans.*, 2017, **46**, 3623–3630.
51 G. Liu, Y. Li, J. Chi, N. Xu, X. Wang, H. Lin, B. Chen and J. Li, *Dalton Trans.*, 2019, **49**, 737–749.
52 Z. H. Jiao, X. L. Jiang, S. L. Hou, M. H. Tang and B. Zhao, *Inorg. Chem.*, 2020, **59**, 2171–2177.
53 Y. Ma, Y. Zhang, X. Li, P. Yang, J. Y. Yue, Y. Jiang and B. Tang, *Anal. Chem.*, 2020, **92**, 3722–3727.
54 G. Chakraborty, P. Das and S. K. Mandal, *ACS Appl. Mater. Interfaces*, 2020, **12**, 11724–11736.
55 X. M. Yin, L. L. Gao, P. Li, R. Bu, W. J. Sun and E. Q. Gao, *ACS Appl. Mater. Interfaces*, 2019, **11**, 47112–47120.
56 X. Z. Song, F. F. Sun, S. T. Dai, X. Lin, K. M. Sun and X. F. Wang, *Inorg. Chem. Front.*, 2018, **5**, 1107–1114.
57 B. X. Dong, Y. M. Pan, W. L. Liu and Y. L. Teng, *Cryst. Growth Des.*, 2017, **18**, 431–440.

58 D. K. Singha, P. Majee, S. Mandal, S. K. Mondal and P. Mahata, *Inorg. Chem.*, 2018, **57**, 12155–12165.
59 F. J. Zhao, G. Zhang, Z. Ju, Y. X. Tan and D. Yuan, *Inorg. Chem.*, 2020, **59**, 3297–3303.
60 L. Wu, C. Huang, B. P. Emery, A. C. Sedgwick, S. D. Bull, X. P. He, H. Tian, J. Yoon, J. L. Sessler and T. D. James, *Chem. Soc. Rev.*, 2020, **49**, 5110–5139.
61 X. Y. Guo, F. Zhao, J. J. Liu, Z. L. Liu and Y. Q. Wang, *J. Mater. Chem. A*, 2017, **5**, 20035–20043.